

A Deep Surrogate Model for Robust and Generalizable Long-Term Blast Wave Prediction

Danning Jing,^{1,2,3} Xinhai Chen*,^{1,2,3} Xifeng Pu,^{1,2,3} Jie Hu,^{1,2,3} Chao Huang,^{4,5} Xuguang Chen,^{1,2,3} Qinglin Wang,^{1,2,3} and Jie Liu^{1,2,3}

¹National Key Laboratory of Parallel and Distributed Computing, National University of Defense Technology, Changsha 410073, China;

²Laboratory of Digitizing Software for Frontier Equipment, National University of Defense Technology, Changsha 410073, China.

³College of Computer Science and Technology, National University of Defense Technology, Changsha 410073, China

⁴CAEP Software Center for High Performance Numerical Simulation, Beijing 100088, China

⁵Institute of Applied Physics and Computational Mathematics, Beijing 100088, China

(*Electronic mail: chenxinhai16@nudt.edu.cn)

(Dated: 23 February 2026)

Accurately modeling the spatio-temporal dynamics of blast wave propagation remains a longstanding challenge due to its highly nonlinear behavior, sharp gradients, and burdensome computational cost. While machine learning-based surrogate models offer fast inference as a promising alternative, they suffer from degraded accuracy, particularly evaluated on complex urban layouts or out-of-distribution scenarios. Moreover, autoregressive prediction strategies in such models are prone to error accumulation over long forecasting horizons, limiting their robustness for extended-time simulations. To address these limitations, we propose RGD-Blast, a robust and generalizable deep surrogate model for high-fidelity, long-term blast wave forecasting. RGD-Blast incorporates a multi-scale module to capture both global flow patterns and local boundary interactions, effectively mitigating error accumulation during autoregressive prediction. We introduce a dynamic-static feature coupling mechanism that fuses time-varying pressure fields with static source and layout features, thereby enhancing out-of-distribution generalization. Experiments demonstrate that RGD-Blast achieves a two-order-of-magnitude speedup over traditional numerical methods while maintaining comparable accuracy. In generalization tests on unseen building layouts, the model achieves an average RMSE below 0.01 and an R^2 exceeding 0.89 over 280 consecutive time steps. Additional evaluations under varying blast source locations and explosive charge weights further validate its generalization, substantially advancing the state of the art in long-term blast wave modeling.

I. INTRODUCTION

A blast wave originates from an explosive source and propagates rapidly through the surrounding environment, exerting intense impulsive loads on structural surfaces within milliseconds. Physically, this process is described as a highly transient, compressible flow characterized by sharp shock fronts and abrupt spatio-temporal variations in overpressure. The propagation dynamics are strongly modulated by urban building layouts, which induce complex wave reflections, diffractions, and localized pressure amplifications, thereby introducing significant nonlinearity and spatial heterogeneity. Accurately characterizing the spatiotemporal evolution of blast waves is therefore critical for reliable structural damage assessment and urban explosion risk mitigation¹⁻³.

Despite its importance, high-fidelity modeling of blast wave propagation remains a longstanding challenge due to its highly nonlinear behavior and sharp gradients^{4,5}. As blast waves propagate through complex environments, they exhibit intricate physical behaviors, such as multi-path reflections and diffractions. These phenomena arise from the evolution of the pressure field across intricate spatial layouts on millisecond time scales. Spatio-temporal coupling further compounds the difficulty of high-fidelity simulations and quantitative analysis, as resolving such transient flow features requires capturing

sharp shock fronts and abrupt gradients.

Numerical methods possess the capacity to resolve transient flow behavior in complex building layouts⁶. However, their iterative solution process leads to prohibitive computational costs, especially when simulating unseen layouts or varying explosion scenarios, each requiring full re-simulation. This inflexibility severely limits their applicability in real-time risk assessment or large-scale scenario exploration. Such limitations highlight the pressing need for efficient surrogate models

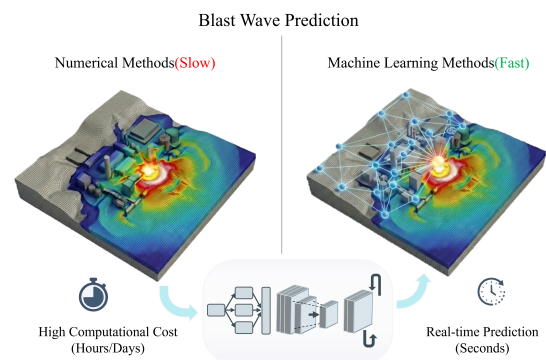


FIG. 1. Machine learning-based surrogate for Blast Wave Prediction

that can balance physical accuracy with computational speed. While offering computational efficiency, empirical methods exhibit a deficit in generalization to real-world urban layouts where structures substantially alter spatio-temporal evolution of blast waves, as they target providing precise parameters mapping for assessing explosion damage^{7,8}.

Recently, machine learning (ML) has emerged as a surrogate for numerical methods in resolving the spatio-temporal evolution of flow fields^{9,10}. As displayed in Fig. 1, the machine learning-based surrogate for blast wave prediction demonstrates a remarkable capacity for flow field resolution. ML methods enable simulation acceleration and have been successfully applied to the prediction of blast load parameters for rapid damage assessment and analysis^{11,12}. For example, Pannell et al.¹³ encoded the physical law that specific impulse monotonically decreases with scaled distance and incidence angle as a monotonicity penalty in the loss function, enhancing accuracy in blast load prediction. This ML-based approach is well-suited for problems with clear, quantifiable physical constraints, yet still lacks generalization to unseen scenarios. Li et al.¹⁴ proposed a machine learning method based on graph neural networks for multi-step spatio-temporal forecasting of overpressure wave propagation. This method fundamentally relies on an autoregressive inference paradigm, where the prediction at each time step serves as input for the next. Although this avoids iterative solving of governing equations and improves computational efficiency, it inevitably accumulates errors during iterative inference from previous predictions, undermining temporal robustness in long-term forecasting and suffering from poor generalization in out-of-distribution urban settings. As summarized in Table I, typical ML methods achieve high efficiency and reasonable spatio-temporal resolution but fall short in long-term robustness and generalization.

TABLE I. Comparative analysis of the proposed RGD-Blast against typical existing methods.

Method	Efficiency	Spatio-temporal Evolution	Long-term Robustness	Generalization
Empirical methods	✓	✗	✗	✗
Numerical methods	✗	✓	✓	✓
ML methods	✓	✓	✗	✗
RGD-Blast (Ours)	✓	✓	✓	✓

To meet the demand for full-process, high-fidelity blast wave simulation, we propose RGD-Blast, a robust and generalizable deep surrogate model for long-term blast wave forecasting. A multi-scale module incorporated in RGD-Blast captures global flow patterns and local boundary interactions, effectively mitigating error accumulation in autoregressive prediction. We introduce a dynamic-static feature coupling mechanism that fuses temporal pressure fields with static source and layout features to improve out-of-distribution (OOD) generalization. Experiments show that RGD-Blast achieves a two-order-of-magnitude speedup over numerical methods while maintaining high fidelity. On unseen urban layouts, it attains an average RMSE below 0.01

and $R^2 > 0.89$ over 280 time steps, and demonstrates robust performance across varying blast source locations and charge weights, significantly extending the forecasting horizon of existing surrogates for rapid structural damage assessment.

II. RELATED WORK

A. Traditional and Machine Learning-based Methods

Accurate modeling of blast wave propagation in complex environments remains a long-standing challenge due to its highly nonlinear dynamics and sharp spatio-temporal gradients^{15,16}. Despite the urgent need for sub-second prediction of unsteady blast wave fields in urban explosions and terrorist attacks, on-site experiments are impractical-being costly, time-consuming, and hazardous, yielding only sparse, incomplete flow field data^{17,18}.

High-fidelity numerical simulations can resolve the spatio-temporal propagation of blast waves and their complex interactions with urban structures, such as reflections and diffractions¹⁹. However, achieving sufficient accuracy demands solving large-scale algebraic systems from discretized governing equations, resulting in computational costs that hinder their use in real-time blast-resistant design and structural response analysis. In contrast, empirical methods offer computational efficiency but rely on idealized assumptions, such as free-field explosions and negligible ground effects, rendering them inadequate for realistic urban environments with intricate layouts²⁰. Consequently, accurate blast wave forecasting directly enables safer building design, robust aircraft protection, and effective post-detonation damage assessment²¹.

Machine learning has emerged as a promising surrogate for blast wave prediction^{22,23}. Early machine learning approaches for blast wave prediction primarily adopted static, parameter-to-load mappings, using a few layout or explosive parameters to predict pointwise peak quantities such as overpressure or impulse²⁴. For instance, Remennikov et al.²⁵ employed parameters such as wall height, standoff distance and barrier position to predict blast loads rapidly, but their model was restricted to a single urban configuration and exhibited sharp accuracy degradation when extrapolating from small-scale training data to real-scale explosions. Even when enhanced with Bayesian uncertainty quantification, the approach proposed by Peng et al.²⁶ was only demonstrated on a 3×3 two-dimensional building cluster, leaving the generalization bottleneck unresolved. These models remain confined to fixed layouts and simplified scenarios (e.g., 2D building clusters or indoor environments²⁷), often predicting only single-point responses based on minimal inputs like scaled distance and incidence angle²⁸. Consequently, they suffer from severe accuracy degradation under distribution shifts-such as extrapolation from micro-scale to real-scale explosions or generalization across unseen urban configurations. Collectively, these efforts show that static mappings of parameters are efficient but limited to single-scenario fitting and exhibit poor generalization across unseen building layouts and explosive charge weights.

TABLE II. Comparison of representative methods for blast wave prediction. RGD-Blast employs a multi-scale module for feature extraction, enabling long-term forecasting ($T = 280$) of the full spatio-temporal pressure field.

Model	Task	Backbone	Static Feature	Dynamic Feature	Output	Horizon (T)
DeNN ²⁸	Load pred.	FCNN	Travel Distances	–	Pointwise Pressure	Single-step
Bayesian DL ²⁶	Load pred.	FCNN	Source, Layout	–	Peak metrics	Single-step
BlastGraphNet ³¹	Load pred.	GNN	Source, Geometry	–	Peak metrics	Single-step
CBlast-Net ²⁰	Curve pred.	RNN/CNN	Time-history Sequence	–	Target Curve	–
UNet variants ³⁸	Field Recon.	CNN	Low-res Field + Mask	–	Super-res Field	Static
PIGN ¹⁶	Field Recon.	GNN	Node Coordinates	–	Complete Field	Static
BGN ¹⁴	ST pred.	GNN	Node Coordinates	Timestep, Pressure	Full-field Pressure	25
GIS-GNN ¹⁷	ST pred.	GNN	Node Coordinates	Pressure	Full-field Pressure	54
RGD-Blast (Ours)	ST pred.	ConvRNN	Distance Field + Layout Mask	Timestep, Pressure	Full-field Pressure	280

Note: Abbreviations: Task types: Load pred. (Prediction of Blast load parameters, e.g., peak overpressure, arrival time, and impulse), Curve pred. (Prediction of pressure-time history curves), Field Recon. (Field reconstruction from sparse or low-resolution data), Backbone types: CNN (Convolutional Neural Network), RNN (Recurrent Neural Network), GNN (Graph Neural Network), FCNN (Fully Connected Neural Network). ST pred. (Spatio-temporal evolution of field variables). “–” indicates that the corresponding feature or capability is not utilized by the model.

B. Towards Full Spatio-Temporal Surrogate Modeling

The pursuit of superior robustness and generalization has driven the development of various deep learning surrogate models for full field of blast wave prediction. Min et al.²⁹ proposed a deep learning model based on a conditional 3D CNN to quickly and accurately predict the peak pressure of blast waves propagating between buildings in urban environments with different spacings, but it failed to capture the full spatio-temporal evolution of blast waves.

Covoni et al.³⁰ proposed a graph neural network model that can quickly predict the transient flow of blast waves in unknown three-dimensional geometries over time and space, and it also showed good generalization in a domain 125 times larger than the training simulation. However, this model exhibits significant error accumulation in its prediction results, with the average prediction error increasing with time steps. Graph-based methods rely on irregular graph construction and sparse neighbour search, making them computationally expensive^{31,32}. In contrast to graph-based methods, convolutional and recurrent architectures have demonstrated both accuracy and efficiency for steady-state prediction, transient wave forecasting and super-resolution reconstruction in the broader fluid-dynamics community^{33–35}.

Achieving high-fidelity spatio-temporal prediction of blast waves requires the ability to simultaneously resolve spatial details and track temporal evolution. Convolutional and recurrent architectures play complementary roles in the spatio-temporal prediction of field variables^{36,37}. However, these models lack a mechanism for feature extraction and struggle to coherently capture both the global flow patterns and local boundary interactions in blast wave propagation. Compounding this issue, these methods cannot reveal the complete propagation path of blast waves in space, the processes of reflection and diffraction, or their systemic impact on the overall structure. This limitation severely undermines their generalization, particularly in OOD scenarios where wave diffraction and reflection patterns differ from the training set.

As shown in Table II, existing models generally rely on

single-feature representations and struggle with OOD scenarios, leading to poor generalization and significant error accumulation in long-term forecasting. To address these limitations, we propose RGD-Blast, a robust and generalizable deep surrogate model for high-fidelity, long-term blast wave forecasting. RGD-Blast ensures robustness by leveraging a multi-scale module for feature extraction in combination with recurrent units to mitigate iterative error accumulation. The model constructs a dynamic-static feature coupling mechanism that integrates dynamic pressure fields with static features, such as source information and building layouts. The proposed model delivers rapid, regular-grid, full spatio-temporal prediction of blast wave propagation while avoiding the computational overhead of graphs. Experimental results demonstrate that RGD-Blast achieves a two-order-of-magnitude speedup over numerical methods. The model demonstrates strong generalization and long-term robustness across unseen layouts, varying blast source locations, and diverse charge weights, significantly extending the forecasting horizon of surrogate models for blast wave prediction.

III. METHODOLOGY

A. Numerical Modeling

Blast wave propagation is modeled as an inviscid, compressible flow, governed by the three-dimensional Euler equations:

$$\frac{\partial \mathbf{U}}{\partial t} + \frac{\partial \mathbf{F}(\mathbf{U})}{\partial x} + \frac{\partial \mathbf{G}(\mathbf{U})}{\partial y} + \frac{\partial \mathbf{M}(\mathbf{U})}{\partial z} = 0, \quad (1)$$

where \mathbf{U} , $\mathbf{F}(\mathbf{U})$, $\mathbf{G}(\mathbf{U})$, and $\mathbf{M}(\mathbf{U})$ are column vectors:

$$\mathbf{U} = \begin{pmatrix} \rho \\ \rho u \\ \rho v \\ \rho w \\ \rho E \end{pmatrix}, \quad \mathbf{F}(\mathbf{U}) = \begin{pmatrix} \rho u \\ P + \rho u^2 \\ \rho v u \\ \rho w u \\ u(\rho E + P) \end{pmatrix}, \quad (2)$$

$$\mathbf{G}(\mathbf{U}) = \begin{pmatrix} \rho v \\ \rho u v \\ P + \rho v^2 \\ \rho v w \\ v(\rho E + P) \end{pmatrix}, \quad \mathbf{M}(\mathbf{U}) = \begin{pmatrix} \rho w \\ \rho u w \\ \rho v w \\ P + \rho w^2 \\ w(\rho E + P) \end{pmatrix},$$

E is the total energy per unit mass:

$$E = e + \frac{u^2 + v^2 + w^2}{2}. \quad (3)$$

In the above equations, x, y, z are the three-dimensional Cartesian coordinates; P, ρ, u, v, w are the pressure, density, x -velocity, y -velocity, and z -velocity of the medium in the flow field; e is the internal energy per unit mass; and t is time.

The equation of state (EOS) is:

$$P = (\gamma - 1)\rho \left(E - \frac{u^2 + v^2 + w^2}{2} \right), \quad (4)$$

$$P = (\gamma - 1)\rho e, \quad (5)$$

where atmospheric air is treated as an ideal gas with an adiabatic index of $\gamma = 1.4$.

To model the detonation process of trinitrotoluene (TNT) numerically, the Chapman-Jouguet (CJ) theory is applied, with the Jones-Wilkins-Lee (JWL) equation of state (EOS) describing the expansion of the resulting products:

$$p = A \left(1 - \frac{\omega}{R_1 V} \right) e^{-R_1 V} + B \left(1 - \frac{\omega}{R_2 V} \right) e^{-R_2 V} + \frac{\omega E_0}{V}, \quad (6)$$

where p represents the pressure of the detonation products; V denotes the relative volume of the detonation products; $A, B, R_1, R_2,$ and ω are parameters of the equation of state; E_0 is the internal energy per unit initial volume. The detailed values of relevant parameters are presented in Table III. It should be

TABLE III. Detonation and JWL equation-of-state parameters for TNT.

Parameter	Symbol (Units)	Value
Detonation velocity	D (m/s)	6930
Density	ρ_0 (kg/m ³)	1630
JWL coefficient A	A (MPa)	3.71×10^5
JWL coefficient B	B (MPa)	3.23×10^3
JWL exponent R_1	R_1	4.15
JWL exponent R_2	R_2	0.95
Gruneisen coefficient	ω	0.3
Internal energy per unit volume	E_0 (MJ/m ³)	7000

noted that the detonation velocity D and initial density ρ_0 do

not appear explicitly in the algebraic form of the JWL equation. They are employed to characterize the Chapman-Jouguet (CJ) state, serving as the initial conditions for the subsequent expansion governed by the JWL equation.

B. Problem Statement: Long-term Blast Wave Forecasting

We formulate the task of long-term blast wave forecasting as an autoregressive prediction problem operating via a sliding window mechanism (Fig. 2). The input window progressively advances by incorporating previous predictions of the model while discarding the oldest frames in the autoregressive process. Notably, once the number of iterations exceeds the sliding window size, the input sequence becomes entirely composed of previously generated outputs. At this stage, the forecasting process is based on the output of the model without requiring further ground-truth data. Specifically, given an initial sequence of length T , the model predicts the spatio-temporal field for step $T + 1$. The sliding window then shifts forward, incorporating this predicted state into the input window while discarding the oldest frame at t_0 to forecast step $T + 2$. This inference method allows RGD-Blast to reconstruct the entire explosion process even when only limited initial observations are available. However, this recursive dependency inherently introduces the challenge of error accumulation. Since each input in the testing phase relies on previous predictions rather than ground-truth data, small numerical deviations at early stages can propagate and amplify through the autoregressive feedback loop, potentially leading to feature inconsistencies or temporal drift in long-term forecasting. To mitigate error

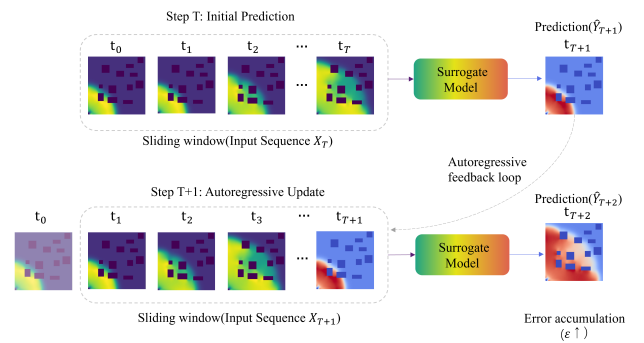


FIG. 2. Autoregressive forecasting process using a sliding window, illustrating the feedback loop and the tendency for error accumulation.

accumulation in blast wave forecasting, a surrogate model capable of feature extraction and robust temporal stabilization is essential. These requirements inform the design of the RGD-Blast model presented in the following section.

C. Overview of RGD-Blast

In this section, we provide a detailed presentation of the multi-scale module designed for extracting dynamic-static features, along with the model structure of the proposed RGD-Blast.

1. Multi-scale Feature Extraction

Models relying on a single feature type often lack sufficient inductive bias, resulting in poor generalization on complex blast wave interactions, particularly obstacle-induced reflections and diffractions. To address these challenges, we incorporate dynamic and static features into the model input. As illustrated in Fig. 3, the input is structured not as simple raw data, but as expanded feature channels composed of dynamic and static features:

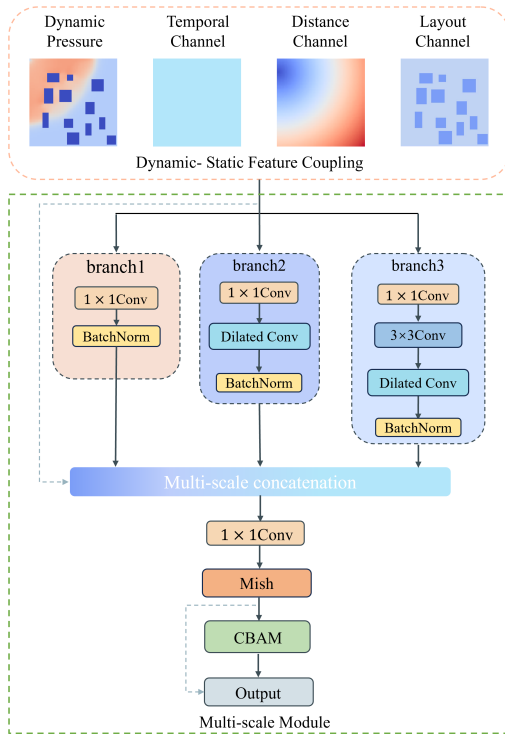


FIG. 3. Multi-scale feature extraction. The input integrates dynamic (pressure, temporal) and static (distance, layout) features into a multi-channel tensor. This rich input is fed into a multi-scale module at the beginning of the encoder.

a. Pressure Channels: Pressure channels capture the evolving dynamic blast wave pressure fields. By leveraging consecutive temporal windows along the time dimension, they simultaneously characterize wave propagation across T time steps, thereby implicitly encoding the velocity and acceleration information of the wavefront.

b. Temporal Channels: Temporal channels provide explicit, dynamic time-awareness. By embedding the elapsed

time since detonation, these channels allow the model to distinguish different blast stages at varying abstraction levels.

c. Distance Channels: Distance channels provide a static spatial prior representing the Euclidean distance from the blast source locations to every spatial coordinate. These establish a structured, global coordinate system with the blast source as its origin, which helps the model discover radial propagation patterns.

d. Layout Channels: Layout channels act as static spatial layout masks representing critical structural layouts. These channels guide attention to local spatial features like building edges where boundary interactions occur.

Crucially, given the heterogeneous nature of these static and dynamic channels, processing them with a single scale is insufficient. Therefore, as shown in the encoder section of Fig. 3, the input tensor is immediately processed by a multi-scale module, which employs three parallel branches with different receptive fields to jointly capture local and long-range dependencies.

Branch 1 employs a 1×1 convolution with batch normalization to extract high-frequency, fine-grained features while preserving spatial resolution. Branch 2 reduces channel dimensionality via 1×1 convolution, then applies a dilated convolution (rate = 2) with batch normalization to capture mid-range contextual patterns at the original resolution. Branch 3 first compresses channels with a 1×1 convolution, aggregates local spatial dependencies through a 3×3 convolution, and further expands the receptive field using a dilated convolution (rate = 2) with batch normalization, enabling modeling of long-range interactions such as diffraction around obstacles.

The outputs from all three branches are concatenated along the channel dimension, forming a fused multi-scale representation. This concatenated feature map is further processed by a 1×1 convolution to adjust the number of channels, followed by a Mish activation function and a convolutional block attention module (CBAM)³⁹ to refine channel and spatial attention. This final step ensures that salient features are enhanced while irrelevant information is suppressed, leading to improved generalization performance.

2. Model Structure

The model structure of the proposed RGD-Blast is illustrated in Fig. 4. The model adopts a spatio-temporal encoder-decoder structure integrated with a convolutional gated recurrent unit (ConvGRU) to capture both spatial correlations and temporal propagation within the input data. The model processes an input sequence with dimensions (B, T, C, H, W) , where B denotes the batch size, T the number of time steps in the input sequence, C the number of dynamic and static channels (e.g., pressure, distance), and $H \times W$ the spatial resolution of each frame. The encoder path progressively reduces spatial resolution by a factor of two from $H \times W$ to $\frac{H}{4} \times \frac{W}{4}$ through alternating multi-scale modules and reduction blocks (Fig. 4a), where s denotes stride and p denotes padding in the diagram. The reduction block compresses the input into high-level abstract features in three parallel branches. The

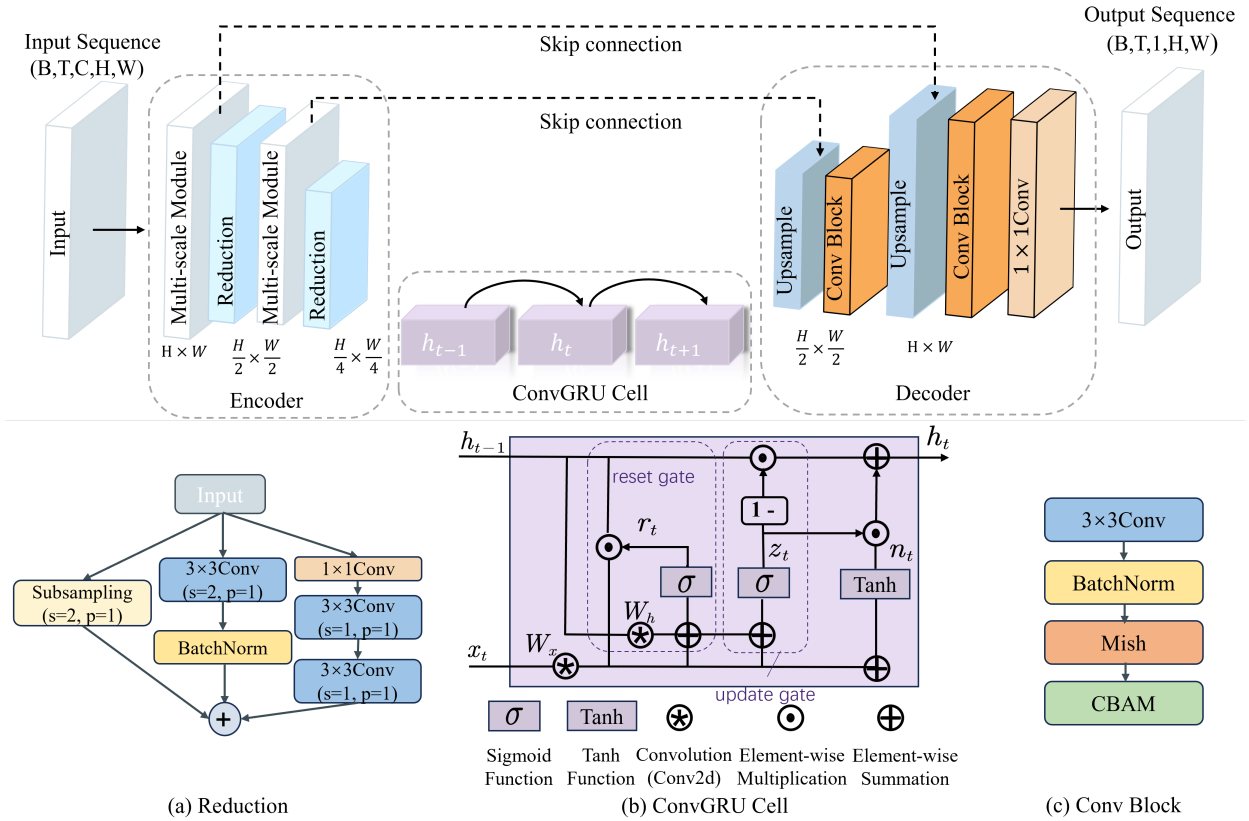


FIG. 4. Overview of the RGD-Blast model, illustrating the encoder-decoder structure and the central ConvGRU for temporal modeling.

first branch applies max pooling; the second performs a single 3×3 convolution followed by batch normalization; the third consists of a 3×3 convolution for channel preservation, followed by two successive 1×1 convolutions and batch normalization. Crucially, instead of concatenating the outputs as in standard inception-style modules⁴⁰, the three branches are fused via element-wise summation, yielding a compact representation that maintains consistent channel dimensions while significantly reducing spatial size and computational cost.

These latent features are then fed into the central ConvGRU cell, which serves as the temporal modeling unit⁴¹. The internal structure of the ConvGRU cell is shown in Fig. 4b, where x_t is the input at time t , h_{t-1} is the previous hidden state, $*$ denotes 2D convolution, \odot is element-wise multiplication, and \oplus is element-wise summation. The update gate z_t controls the balance between retaining past information and incorporating new inputs, while the reset gate r_t determines whether to ignore historical context when computing the new candidate state. The cell computes update and reset gates using convolutional operations to selectively integrate new inputs and preserve relevant historical information, while mitigating error accumulation during autoregressive forecasting.

The decoder reconstructs the spatio-temporal field by progressively upsampling the latent features back to the original resolution $H \times W$, using alternating upsampling and convolution blocks (Fig. 4c). Nearest interpolation is used for upsam-

pling, and long-range skip connections concatenate encoder features at matching resolutions to preserve fine-grained spatial details. Each convolution block consists of a 3×3 convolution, batch normalization, Mish activation, and the standard CBAM. The final output sequence of shape (B, T, C, H, W) is produced via a 1×1 convolution layer.

IV. EXPERIMENTAL RESULTS

A. Experimental Setup

This study constructs three distinct explosion scenarios using numerical methods based on computational fluid dynamics (CFD) to evaluate the spatio-temporal generalization of RGD-Blast (Fig. 5). All scenarios are simulated within a consistent computational domain of $64 \times 64 \times 10$ m (x, y, z). The results are acquired as 2D horizontal slices projected from these 3D scenes at a specific height ($z = 3$ m) aligned with the plane of the blast source, and partitioned into training and testing cases at a 9:1 ratio. This setup is designed to assess model performance across the entire explosion from the initial to the final time step. Each simulation covers a total duration of 0.15 s, resulting in 290 time steps per case. Details of each scenario are provided below.

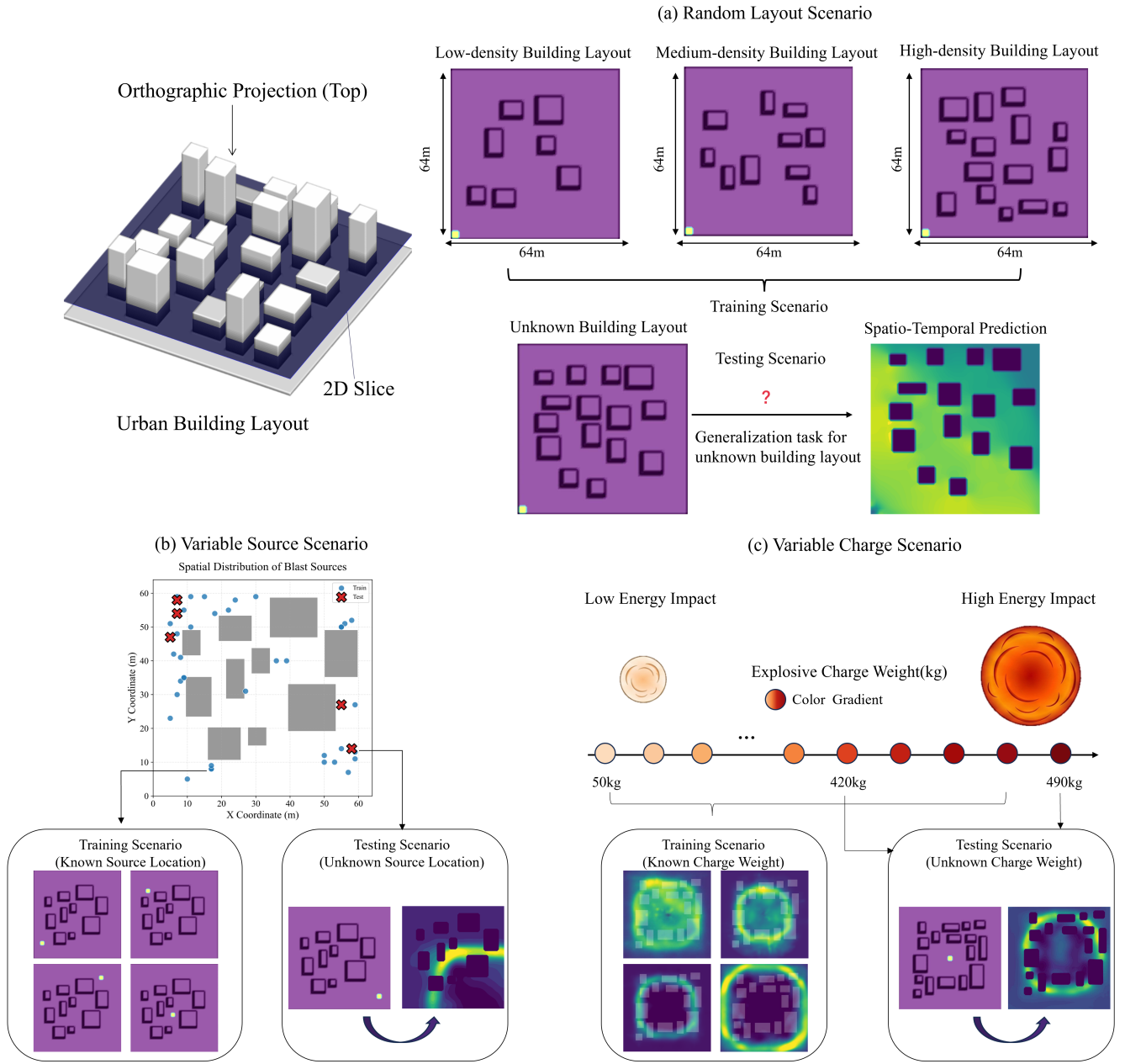


FIG. 5. Overview of spatio-temporal generalization tasks with different training and testing scenarios for RGD-Blast. (a) Generalization task for unseen layouts with random buildings. (b) Generalization task for unseen source weights, where the model is trained on known sources and tested on unknown ones. (c) Generalization task for unseen explosive charge weights, testing the model’s adaptability to varying explosive charge weights.

a. Random Layout Scenario The random layout scenario (Fig. 5a) is designed to evaluate the generalization to unknown spatial layouts with diverse rectangular buildings. It comprises 50 cases, each containing 6 to 15 randomly generated rectangular buildings with planar dimensions ranging from 5 to 10m and heights between 1 and 3m. A minimum clearance of 2m is enforced between any two buildings as well as between buildings and the domain boundaries. All layouts are generated using fixed random seeds to ensure re-

producibility. In this task, the model is trained on a subset of these layouts and evaluated on completely unseen building layouts to test its adaptability to new layouts. The source parameters are standardized with an explosive charge weight of 200 kg and the blast source located at (0, 0, 3 m).

b. Variable Source Scenario In the variable source scenario (Fig. 5b), 50 cases are generated with different blast source locations. These cases are set with an explosive charge weight of 200 kg.

c. Variable Charge Scenario To ensure richness and variability, 45 charge weights (50 kg, 60 kg, ..., 490 kg) were designed in the variable charge scenario (Fig. 5c). In the numerical method, the total number of time steps required to complete each simulation varies from 273 to 317. This variation stems from the internal time-step shedding mechanism of the solver, which dynamically adjusts the step size Δt to satisfy the stability criterion as the blast wave velocity increases with larger charge weights. The blast source is located at (32 m, 32 m, 3 m).

B. Implementation Details

1. Training Procedures

The proposed RGD-Blast is implemented using the PyTorch framework. To enhance temporal modeling, training data are structured into sliding windows using 10 consecutive timesteps to predict the next, with samples randomly shuffled. Input pressure fields are normalized to the range $[0, 1]$ using global min-max normalization. The model is optimized using the Adam optimizer with an initial learning rate of 5×10^{-4} and a weight decay of 10^{-3} , and a batch size of 32. All experiments are conducted on a single NVIDIA RTX 4090 GPU. Furthermore, to guide the training process with physical laws, the model output is subjected to physics-informed constraints, where Scharr filters are applied to compute necessary spatial derivatives (D_x, D_y).

$$D_x = \begin{bmatrix} -3 & 0 & 3 \\ -10 & 0 & 10 \\ -3 & 0 & 3 \end{bmatrix}, \quad D_y = \begin{bmatrix} -3 & -10 & -3 \\ 0 & 0 & 0 \\ 3 & 10 & 3 \end{bmatrix}. \quad (7)$$

The optimization employs a composite loss function:

$$\begin{aligned} L_{\text{data}} &= \frac{1}{N} \sum_{i=1}^N |P_{\text{pred}}^{(i)} - P_{\text{true}}^{(i)}|, \\ L_{\text{grad}} &= \frac{1}{N} \sum_{i=1}^N \left(|\nabla_x P_{\text{pred}}^{(i)} - \nabla_x P_{\text{true}}^{(i)}| + |\nabla_y P_{\text{pred}}^{(i)} - \nabla_y P_{\text{true}}^{(i)}| \right), \\ L_{\text{total}} &= \lambda_1 L_{\text{data}} + \lambda_2 \cdot L_{\text{grad}}, \end{aligned} \quad (8)$$

where L_{data} ensures pixel-level accuracy, and L_{grad} represents the gradient loss. The coefficients λ_1 and λ_2 balance the contributions of data fidelity and physics-informed regularization. In our experiments, we set $\lambda_1 = 1.0$ and $\lambda_2 = 0.8$. $P_{\text{true}}^{(i)}$ and $P_{\text{pred}}^{(i)}$ represent the ground-truth and model-predicted pressure fields (of shape $H \times W$) for the i -th out of N spatio-temporal samples, respectively.

The spatial gradients of the pressure field are approximated using fixed Scharr operators:

$$\nabla_x P = P * D_x, \quad \nabla_y P = P * D_y, \quad (9)$$

where $*$ denotes convolution. These kernels are implemented as non-trainable convolutional layers. Compared to basic central finite-difference operators (e.g., using $[-1/2, 0, 1/2]$ for first-order derivatives), the Scharr operators provide superior

rotational invariance and detail sensitivity, which are critical for capturing the sharp fronts and complex changes of blast waves.

2. Evaluation Metrics

To quantitatively assess the spatio-temporal prediction accuracy, we employ three primary metrics: root mean square error (RMSE) for absolute deviation, mean absolute percentage error (MAPE) for relative accuracy in high-pressure regions, and the coefficient of determination (R^2) to evaluate the overall goodness-of-fit. These metrics collectively validate the model's fidelity in predicting both the magnitude and the dynamic propagation of the blast field.

C. Results and Discussion

1. Prediction of Pressure Field

In this subsection, we evaluate the capability of the proposed model for long-term forecasting of blast wave pressure fields. Through a comprehensive comparison with existing models, we demonstrate the performance of our model in predicting spatio-temporal pressure fields on the test set. As illustrated in Fig. 6, we first visualize the spatio-temporal pressure fields of blast waves in random building layouts at fixed intervals of 50 time steps. The predicted results are validated against data obtained through high-fidelity numerical methods as ground truth. The quantitative error statistics across 280 timesteps are summarized in Table IV. A comparative analysis with baseline models reveals that RGD-Blast maintains high fidelity across 280 unseen time steps. Specifically, RGD-Blast achieves the lowest average MAPE (1.93%) and average RMSE (0.0048), significantly outperforming FNO, which fails in long-term extrapolation with an average MAPE of 73.09%. Furthermore, the minimum R^2 of 0.8928 for RGD-Blast confirms its robustness in capturing peak pressure variations, whereas the baselines exhibit a sharp decline in robustness.

TABLE IV. Performance comparison of different models in random building layouts across 280 timesteps.

Model	MAPE _{max}	MAPE _{avg}	RMSE _{max}	RMSE _{avg}	R^2_{min}
FNO ⁴²	86.38	73.09	0.1856	0.1517	-37.32
E3D-LSTM ⁴³	5.79	3.63	0.0132	0.0093	0.7336
Our Model	5.43	1.93	0.0106	0.0048	0.8928

As illustrated in Fig. 7 and 8, we visualize the spatio-temporal pressure fields of blast wave at a test source location of (7, 54) and a test charge weight of 490 kg. For the variable charge weight scenario, the blast source is fixed at the center of the domain. Due to the increased explosive charge weight, the blast wave propagates more rapidly and reaches the domain boundaries within approximately 100 time steps.

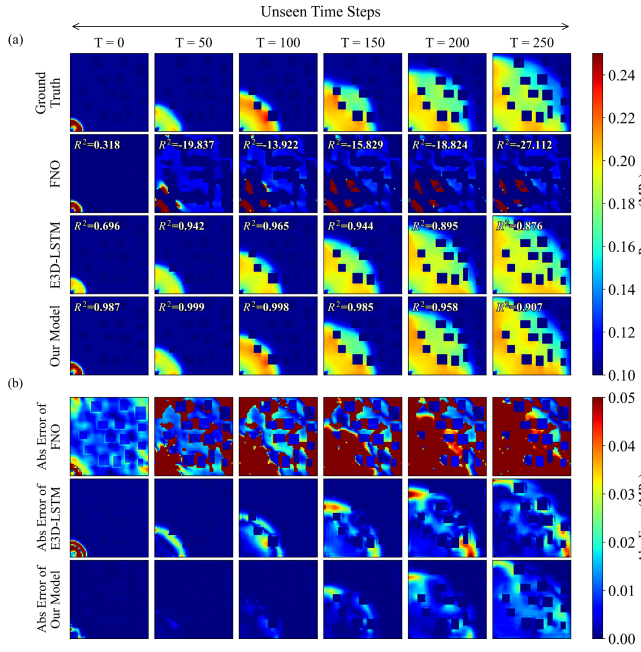


FIG. 6. Comparison of blast wave pressure field predictions and absolute errors across unseen time steps. (a) Spatio-temporal evolution of predicted pressure fields by FNO, E3D-LSTM, and the proposed model, compared to high-fidelity ground truth in a random building layout. R^2 values are annotated for each prediction at selected time steps to indicate long-term forecasting accuracy. (b) Corresponding absolute error results relative to the ground truth, illustrating the spatial distribution of discrepancies. Columns from left to right correspond to time steps $T = 0, 50, 100, 150, 200$, and 250 , demonstrating the superior robustness and generalization of our model under out-of-distribution conditions.

Beyond this point, further temporal comparisons lose physical relevance. Therefore, for this scenario, we report results only over the first 100 time steps, which fully capture the physically meaningful phase of blast wave propagation.

TABLE V. Performance comparison of different models at test source (7, 54) across 280 timesteps.

Model	MAPE _{max}	MAPE _{avg}	RMSE _{max}	RMSE _{avg}	R^2_{\min}
FNO	63.55	57.33	0.0688	0.0598	-920.03
E3D-LSTM	2.30	1.46	0.0178	0.0028	0.1395
Our Model	0.92	0.73	0.0040	0.0011	0.6903

The quantitative metrics summarized in Table V demonstrate that RGD-Blast exhibits robustness to shifts in the source location. Specifically, our model achieves a low average MAPE of 0.73%, which is superior to E3D-LSTM (1.46%) and FNO (57.33%). The RGD-Blast model maintains high fidelity in resolving the initial wavefront expansion and the subsequent complex diffraction around buildings. Notably, even during the most challenging phases of pressure reflection, our model preserves an R^2 of at least 0.6903.

As presented in Table VI, the performance comparison with

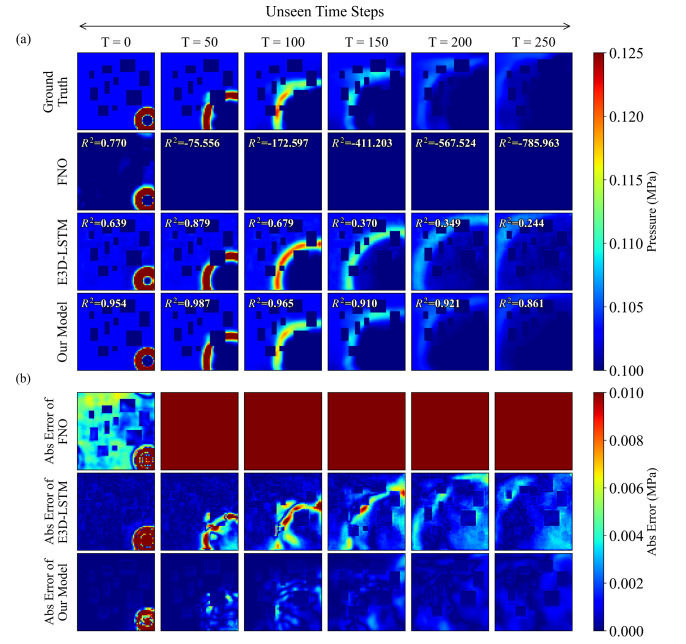


FIG. 7. Comparison of blast wave pressure fields between the ground truth and predictions by various models across unseen time steps with a source location. (a) Predicted pressure fields by FNO, E3D-LSTM, and our model versus ground truth. (b) Corresponding absolute error distributions.

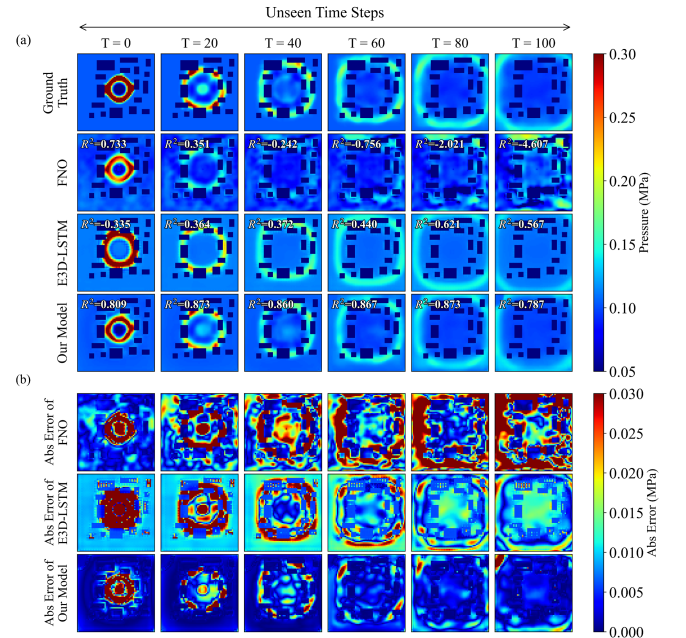


FIG. 8. Comparison of blast wave pressure fields between the ground truth and predictions by various models across unseen time steps with a charge weight. (a) Predicted pressure fields. (b) Corresponding absolute error distributions.

TABLE VI. Performance comparison of different models at charge weight of 490 kg across 100 timesteps.

Model	MAPE _{max}	MAPE _{avg}	RMSE _{max}	RMSE _{avg}	R^2_{\min}
FNO	26.87	16.07	0.0429	0.0316	-4.6068
E3D-LSTM	33.81	10.44	0.0920	0.0267	-0.2248
Our Model	12.37	4.13	0.0363	0.0095	0.7869

existing surrogate models is evaluated at a test charge weight of 490 kg. In this high-intensity scenario, RGD-Blast continues to achieve an average MAPE of 4.13% and an average RMSE of 0.0095. In contrast, both FNO and E3D-LSTM exhibit a substantial loss of accuracy, with their minimum R^2 values dropping into negative territory (-4.6068 and -0.2248 , respectively), indicating a failure to track the sharp pressure gradients associated with larger explosive yields. RGD-Blast maintains a robust R^2 of at least 0.7869, demonstrating its superior ability to scale with varying charge weights. This performance advantage confirms that the integration of source information as a static feature, coupled with the multi-scale module, allows the model to capture the underlying physical laws of blast wave propagation rather than over-fitting to specific source locations or charge weights.

Table VII compares the total computational time for generating spatio-temporal blast pressure sequences containing 280 time steps between the high-fidelity numerical method and RGD-Blast. The task corresponds to the complex cases with the same experimental settings as the random building layout scenario. The quantitative results verify the efficiency advantage of RGD-Blast with a two-order-of-magnitude speedup, reducing the total time from over 2400 seconds to approximately 12.77 seconds.

TABLE VII. Computational efficiency comparison between the numerical method and RGD-Blast for the random building layout scenario.

Model	Total Time (s)	Time per Step (s)	Speedup
Numerical method	2415.91	8.63	1×
RGD-Blast (Ours)	12.77	0.046	$\sim 189\times$

2. Pressure-time histories

We further probe pressure-time histories across three OOD scenarios: a new layout (case 38), a new source location at (7, 54), and a test charge weight of 490 kg. As illustrated in Fig. 9, RGD-Blast accurately reconstructs the nonlinear pressure-time histories, including critical parameters such as arrival time, peak magnitude of pressure, and positive phase duration.

The model precisely tracks the sharp pressure jump at the shock front (P0), reflecting its spatial sensitivity to initial wave expansion. RGD-Blast reproduces the peaks and delayed arrivals in the diffraction zone (P1), confirming its internalized

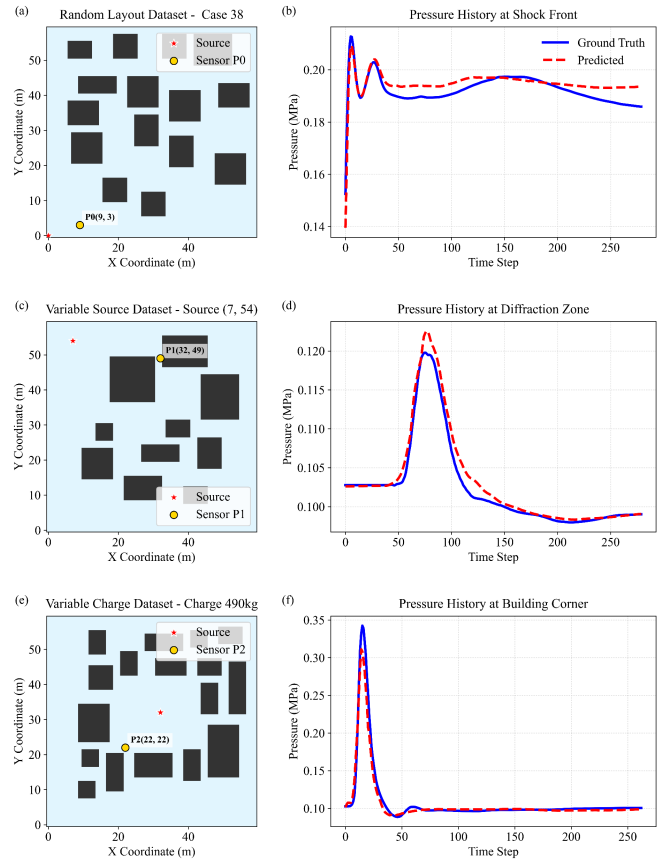


FIG. 9. Pressure-time histories predicted by RGD-Blast under three out-of-distribution (OOD) scenarios: (a,b) random layout, (c,d) variable source location, and (e,f) variable charge weight. The model accurately captures the shock front arrival, peak pressure, and diffraction effects, demonstrating robust generalization across unseen urban configurations and explosive scales.

understanding of spatial source configurations. Notably, the model maintains numerical stability at structural discontinuities (P2), successfully capturing the reflected shock enhancements even under extrapolated energy scales. Minor phase discrepancies in the late-stage decay are attributed to error accumulation during autoregressive predictions. However, the high-fidelity reconstruction of primary peaks and impulses ensures the model’s reliability for structural damage analysis.

D. Robustness and Generalization Analysis

1. Long-term Robustness Analysis

To rigorously evaluate the temporal stability of RGD-Blast, we examine its autoregressive performance across extended 280 time steps involving unseen blast scenarios. As illustrated in Fig. 10, we employ a distributional visualization approach, incorporating mean trends, shaded uncertainty bands, and numerical scatter points from multi-cases.

Notably, while the E3D-LSTM baseline exhibits inherent

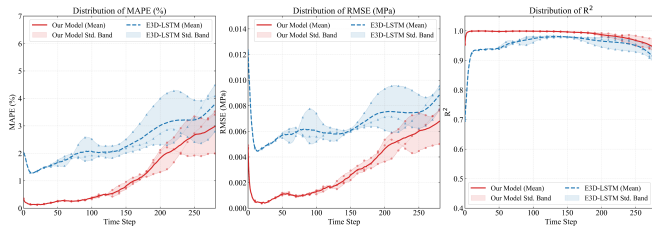


FIG. 10. Comparison of autoregressive prediction errors across different models. Panels show the distribution of MAPE (%), RMSE (MPa), and R^2 over a 280-timestep horizon, respectively. The solid lines represent mean values, and shaded regions denote the deviation band.

and significant fluctuations during the early transient stages, RGD-Blast maintains a stable error performance from the onset. This early-stage precision is of importance for blast engineering, as it is related to initial overpressure fluctuations and peak characteristics. Although, FNO-based models are employed in previous baselines, we excluded them from this long-term stability comparison because preliminary tests revealed that FNO-based models suffer from severe numerical divergence in multi-step autoregressive prediction for these complex scenarios, which would compromise the clarity and scale of the comparative analysis.

Although the error envelopes of different models may partially overlap in later stages, RGD-Blast consistently delivers superior accuracy when evaluated on identical OOD cases. Specifically, the model maintains a robust R^2 above 0.90 throughout the 280-step autoregressive prediction. Furthermore, the slight error growth in the late-stage decay phase has negligible impact on downstream engineering applications, such as peak overpressure assessment and structural damage analysis, which are predominantly dictated by the high-fidelity results of the initial phase.

2. Generalization

The generalization capability of our model was quantified through various OOD testing scenarios involving new building layouts, unseen blast source locations, and varying explosive charge weights. As illustrated in Fig. 11, we evaluated the model across multiple unseen building layouts, where cases 7, 45, and 46 denote the specific indices of distinct layouts. The visual comparison in Fig. 11, where each case contains two rows (ground truth and prediction), demonstrates that the model accurately reconstructs the complex wave-obstacle interactions in these unseen layouts. Quantitatively, as summarized in Table VIII, the model maintains its precision across all new building layouts, with average MAPE below 1.30% and minimum R^2 values consistently exceeding 0.91, demonstrating robust spatial generalization.

Furthermore, the model’s generalization to change of the explosion source was evaluated. As illustrated in Fig. 12, we tested RGD-Blast across multiple unseen source locations, including coordinates (7,58), (5,47), and (55,27). The visual

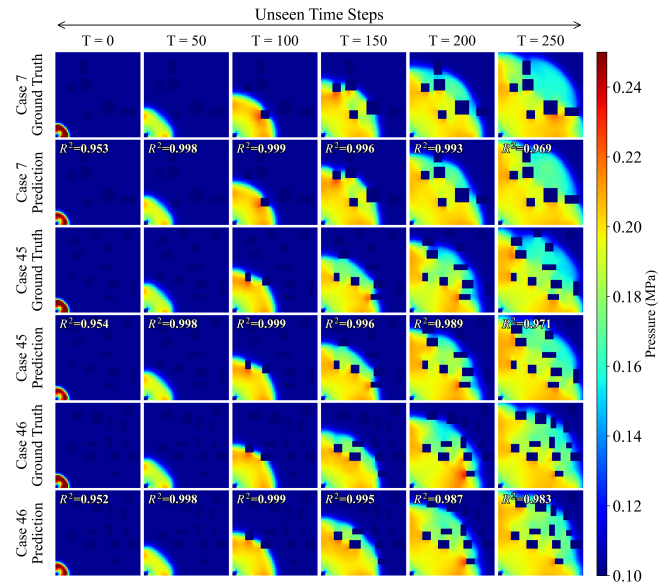


FIG. 11. Performance comparison of testing at untrained new building layout cases

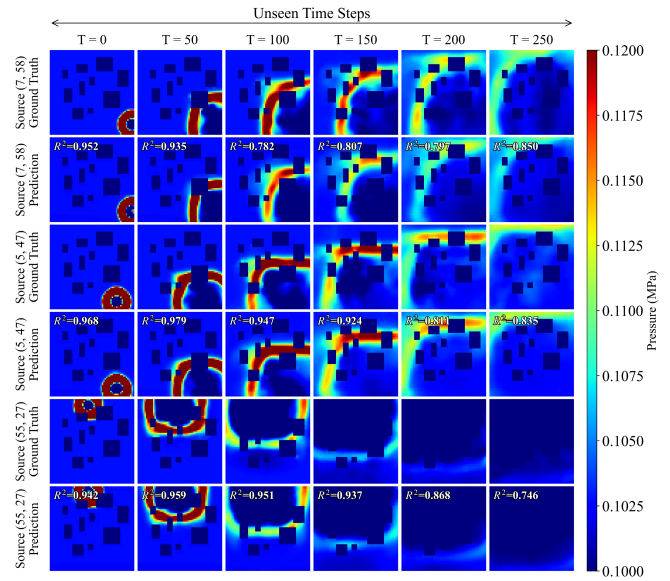


FIG. 12. Performance comparison of testing at untrained new source locations

results confirm that the model accurately captures the directional propagation and reflection effects triggered by different source-layout spatial configurations. Error statistics in Table VIII reveal that the average MAPE remains below 1.00% for all tested coordinates.

As visualized in Fig. 13, the model’s robustness across varying energy intensities was validated by testing extrapolated charge weights of 420 kg and 490 kg. Quantitatively, as summarized in Table VIII, the model maintains high-fidelity predictions even in these high charge weight OOD cases, with an average MAPE below 4.80% and a robust R^2 consistently

TABLE VIII. Generalization performance of RGD-Blast across unseen building layouts, source locations, and explosive charge weights.

Generalization Case	MAPE _{max}	MAPE _{avg}	RMSE _{max}	RMSE _{avg}	R^2_{max}	R^2_{min}
New Layout (Case 7)	3.74	1.10	0.0081	0.0029	0.9997	0.9169
New Layout (Case 45)	3.95	1.30	0.0083	0.0032	0.9997	0.9223
New Layout (Case 46)	3.28	1.19	0.0083	0.0032	0.9997	0.9547
Unseen Source (7, 58)	1.29	0.99	0.0036	0.0018	0.9955	0.7560
Unseen Source (5, 47)	1.15	0.90	0.0036	0.0016	0.9955	0.8331
Unseen Source (55, 27)	1.07	0.81	0.0054	0.0013	0.9838	0.4501
Charge Weight 420 kg	9.79	4.74	0.0310	0.0105	0.9509	0.7274
Charge Weight 490 kg	12.37	4.13	0.0363	0.0095	0.9589	0.7961

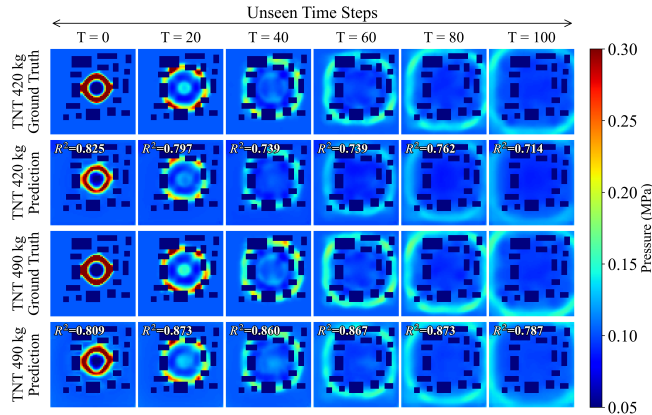


FIG. 13. Performance comparison of testing at untrained new charge weights

above 0.72. In particular, the R^2_{max} reaching 0.9589 for the 490 kg case confirms that the multi-scale module remains numerically stable even under extreme transient conditions. These results across unseen layouts, source locations, and OOD charge weights collectively demonstrate that RGD-Blast does not merely interpolate within the training distribution, but obtains superior robustness and generalization.

E. Ablation Study

1. Dynamic-Static Features Analysis

To justify the effectiveness of the proposed dynamic-static feature coupling mechanism, ablation experiments are conducted by selectively removing feature channels. The experimental settings include three variants, each missing specific features: distance channel, time channel, and static layout channel. The comparison results are presented in Fig. 14 and Table IX. The omission of distance and time channels results in the lowest R^2 scores and performance failure. Additionally, the variant without the static layout channel fails to resolve interaction effects such as reflection and diffraction, leading to a significant accuracy drop compared to the full model. In contrast, the full model achieves the optimal performance across

all metrics, validating that the coupling of dynamic-static features is essential to enhance generalization and mitigate error accumulation in OOD scenarios.

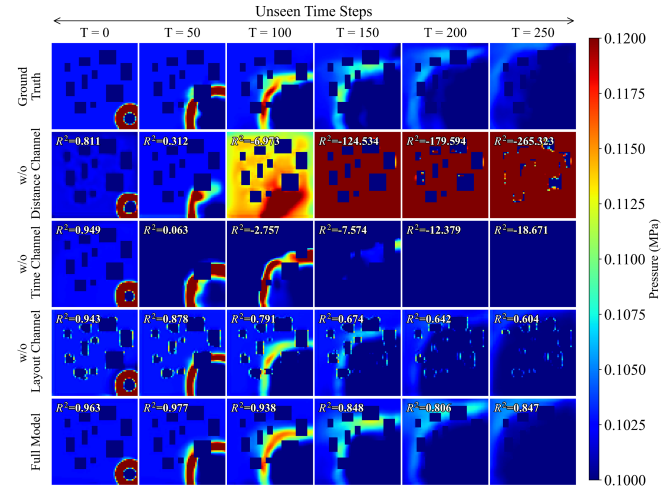


FIG. 14. Ablation study of dynamic-static feature coupling on test source locations. The first row presents the ground truth. The subsequent rows display predictions from variants excluding specific features (distance channel, time channel, and static layout channel) compared against the full model over unseen time steps.

TABLE IX. Performance comparison of ablation study for feature channels at test source (7, 54) across the 280-timestep forecasting horizon.

Model	MAPE _{max}	MAPE _{avg}	RMSE _{max}	RMSE _{avg}	R^2_{min}
w/o Distance Channel	33.65	19.98	0.0342	0.0218	-318.5
w/o Time Channel	18.78	14.78	0.0194	0.0160	-93.33
w/o Layout Channel	1.28	1.07	0.0071	0.0020	0.5938
Full Model	0.92	0.73	0.0040	0.0011	0.6903

2. Contribution of Spatio-Temporal Modules

To rigorously verify the contribution of each component of RGD-Blast, we implement a series of ablation experiments by

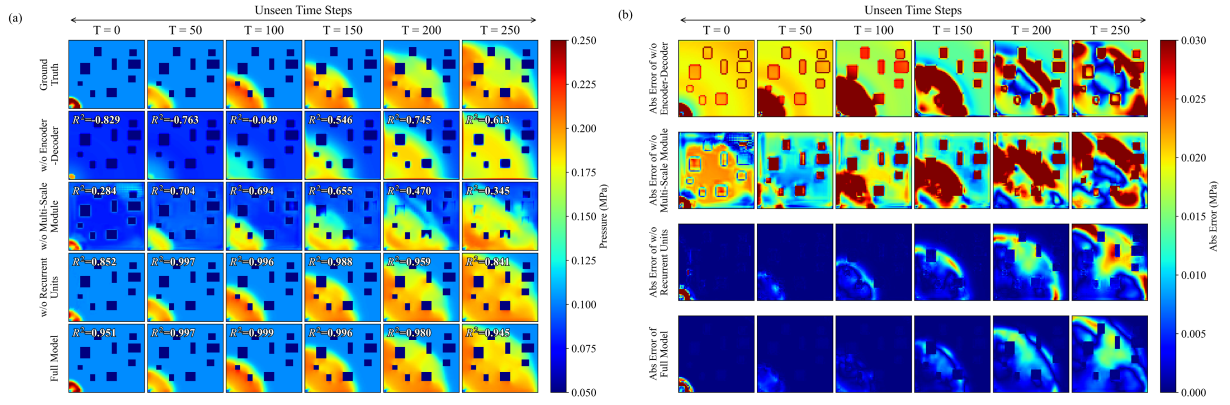


FIG. 15. Comparative ablation study of RGD-Blast across unseen time steps. (a) Predicted pressure fields with R^2 values at selected time steps for the full model and three ablated variants: w/o encoder-decoder, w/o multi-scale module, and w/o recurrent units. (b) Absolute error maps showing spatial distribution of prediction errors for each variant over time.

systematically modifying the core model.

The specific configurations of the ablation variants are defined as follows:

a. w/o Encoder-Decoder: The hierarchical downsampling and upsampling pathways are entirely removed. The input features are directly mapped to the output space using 1×1 convolutions at the original resolution.

b. w/o Multi-Scale Module: The three receptive-field branches within the multi-scale module are replaced by standard 3×3 convolutional layers. This setup isolates the effect of the parallel receptive fields in capturing sharp gradients.

c. w/o Recurrent Units: The ConvGRU cells are entirely bypassed. The middle latent processing stage is removed, and the spatial features extracted by the encoder are fed directly into the decoder at each time step.

As summarized in Table X and Fig. 15, the full model maintains a superior R^2_{\min} of 0.9165 and the lowest error metrics across the 280-timestep forecasting horizon.

These results confirm that the collaborative contribution between the multi-scale module and the recurrent units is critical for mitigating error accumulation and ensuring long-term forecasting robustness.

TABLE X. Ablation study of our model across a 280-timestep forecasting horizon, evaluating contributions of model components using MAPE, RMSE, and R^2 metrics.

Model	MAPE _{max}	MAPE _{avg}	RMSE _{max}	RMSE _{avg}	R^2_{\min}
w/o Encoder-Decoder	22.01	16.61	0.0381	0.0273	-1.5901
w/o Multi-Scale Module	16.41	13.71	0.0290	0.0222	-0.0759
w/o Recurrent Units	6.42	2.38	0.0133	0.0055	0.8110
Full Model	3.65	1.37	0.0080	0.0035	0.9165

F. Damage Assessment

To evaluate the engineering utility of RGD-Blast, we applied the predicted high-fidelity fields to a rapid structural

damage assessment for the ground structures shown in Fig. 16a. According to the P - I damage criteria for structures, the degree of destruction is quantified by a series of hyperbolic curves as summarized in Table XI and Fig. 16b, where the P - I space is partitioned into distinct regions-minor damage, moderate damage, severe damage, and total destruction³¹. The positive peak overpressure Δp_+ is determined by traversing all time steps to record the maximum difference between the predicted total pressure P in Section IV C 1 and the initial atmospheric pressure P_i (102,759 Pa). The positive phase impulse I_+ is calculated by integrating the overpressure over the positive duration of the pressure-time history in Section IV C 2.

TABLE XI. P - I damage criteria expressed in hyperbolic form for varying damage levels.

Damage Levels	P - I damage criteria (Δp_+ kPa, I_+ kPa·s)
Minor damage	$(\Delta p_+ - 6.205)(I_+ - 0.517) = 3.185$
Moderate damage	$(\Delta p_+ - 11.721)(I_+ - 0.931) = 10.934$
Severe damage	$(\Delta p_+ - 24.821)(I_+ - 1.827) = 45.161$
Total destruction	$(\Delta p_+ - 48.263)(I_+ - 3.068) = 147.367$

The visual alignment between the predicted damage contours and the diverse building layouts (Fig. 16c) indicates that RGD-Blast maintains strict physical consistency even under rapid inference. Specifically, the model correctly identifies the total destruction zones near the source, while transitioning to minor damage levels as the blast energy dissipates and diffracts. Furthermore, the quantitative analysis in Figure 16(d) demonstrates the building shielding effect. By comparing the area percentage statistics across different cases, it is evident that more complex and denser building layouts lead to a higher proportion of none and minor damage levels. For instance, in layouts with high building density (case 38), the safe zones occupy approximately 43.7% of the total area, which is significantly higher than in more open building layouts. This high-fidelity damage assessment capability highlights the engineering utility of RGD-Blast for emergency response and structural protective design.

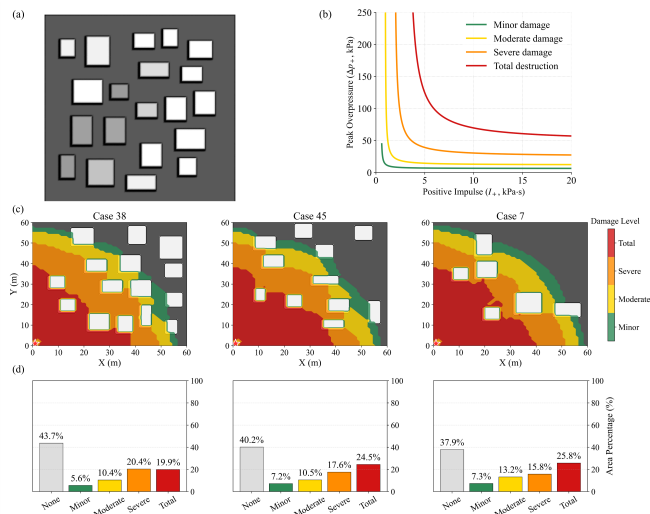


FIG. 16. Structural damage assessment based on $P-I$ criteria. (a) Building layout. (b) $P-I$ damage curves. (c) Damage assessment across multiple unseen layouts. (d) Quantitative statistics of damage area percentages.

V. CONCLUSION

In this study, we develop RGD-Blast, a robust and generalizable deep surrogate model specifically engineered to address the accuracy degradation in long horizons and OOD scenarios for blast wave forecasting. To mitigate autoregressive error accumulation, we incorporated a multi-scale module coupled with recurrent units to capture both global flow distributions and local boundary details for long-term robustness. By implementing a dynamic-static feature coupling mechanism, the model effectively integrates dynamic physical variables with static features, significantly enhancing its generalization. Experimental results demonstrate that RGD-Blast achieves a two-order-of-magnitude speedup over traditional numerical methods without compromising accuracy. Crucially, the model exhibits generalization across unseen building layouts, maintaining an average RMSE below 0.01 and R^2 exceeding 0.89 over 280 time steps. Furthermore, RGD-Blast exhibits superior long-term forecasting robustness across varying blast source locations and explosive charge weights, enabling rapid damage assessment for ground structures. Future work will extend the model to three-dimensional urban environments and structural response analysis.

¹M. tao Zhang, Y. Pei, X. Yao, and Y. xue Ge, “Damage assessment of aircraft wing subjected to blast wave with finite element method and artificial neural network tool,” *Defence Technology* **25**, 203–219 (2023).

²Y. Liu, Q. Peng, Z. Fan, Y. Zheng, H. Wang, D. Wu, Y. Wei, and X. Liu, “Safety assessment of explosion fragment projection in a wind field,” *Journal of Loss Prevention in the Process Industries* **94**, 105544 (2025).

³B. Li, B. Feng, and L. Chen, “Adaptive feature-extraction graph network for physical systems: Prediction of inviscid compressible flow in urban explosion,” *Engineering Structures* **345**, 121482 (2025).

⁴O. S. Isaac, O. G. Alshammari, and E. G. P. D. C. E. Rigby, “Blast wave interaction with structures – an overview,” *International journal of protective structures* **14**, 584–630 (2023).

⁵A. Ratcliff, S. Rigby, S. Clarke, and S. Fay, “A review of blast loading in the urban environment,” *Applied Sciences* **13** (2023), 10.3390/app13095349.

⁶G. Valsamos, M. Larcher, and F. Casadei, “Beirut explosion 2020: A case study for a large-scale urban blast simulation,” *Safety Science* **137**, 105190 (2021).

⁷V. Feldgun, Y. Karinski, and D. Yankelevsky, “A simplified model with lumped parameters for explosion venting simulation,” *International Journal of Impact Engineering* **38**, 964–975 (2011).

⁸A. Gautier, I. Sochet, and S. Courtiaud, “Analysis of Shock Wave Interaction with an Obstacle by Coupling Pressure Measurements and Visualization,” *Sensors* **22**, 3325 (2022).

⁹W. Chen, X. Chen, Q. Xiao, H. Yang, J. Tu, L. Jiang, and J. Liu, “A static-dynamic feature coupling framework for spatiotemporal multiphase flow prediction in heterogeneous reservoirs,” *Physics of Fluids* **37** (2025).

¹⁰Q. Xiao, X. Chen, H. Yang, C. Gong, and J. Liu, “St-flownet: A lightweight framework for long-term spatio-temporal flow field prediction,” *Neural Networks* **195**, 108243 (2026).

¹¹F. Xing, J. Li, Z. Tao, F. Liu, and Y. Tan, “Modeling dynamic gas-liquid interfaces in underwater explosions using interval-constrained physics-informed neural networks,” *Physics of Fluids* **37** (2025).

¹²M. Zahedi and S. Golchin, “Prediction of blast loading on protruded structures using machine learning methods,” *International Journal of Protective Structures* **0**, 1–19 (2022).

¹³n. P. J. J. Pannell, S. Rigby, “Physics-informed regularisation procedure in neural networks: An application in blast protection engineering,” *International Journal of Protective Structures* **13** **1**, 555 – 578 (2022).

¹⁴Q. Li, Y. Wang, W. Chen, L. Li, and H. Hao, “Machine learning prediction of bleve loading with graph neural networks,” *Reliability Engineering & System Safety* **241**, 109639 (2024).

¹⁵D. V. Gaitonde and M. C. Adler, “Dynamics of three-dimensional shock-wave/boundary-layer interactions,” *Annual Review of Fluid Mechanics* **55**, 291–321 (2023).

¹⁶J.-Z. Peng, Z.-Q. Wang, X. Rong, M. Mei, M. Wang, Y. He, and W.-T. Wu, “Rapid and sparse reconstruction of high-speed steady-state and transient compressible flow fields using physics-informed graph neural networks,” *Physics of Fluids* **36** (2024).

¹⁷J. Shi, J. Li, H. Zhang, B. Xie, Z. Xie, Q. Yu, and J. Yan, “Real-time gas explosion prediction at urban scale by gis and graph neural network,” *Applied Energy* **377**, 124614 (2025).

¹⁸R. Hajek, M. Foglar, and J. Fladr, “Influence of barrier material and barrier shape on blast wave mitigation,” *Construction and Building Materials* **120**, 54–64 (2016).

¹⁹D. Mohotti, K. Wijesooriya, and S. Weckert, “A simplified approach to modelling blasts in computational fluid dynamics (cfd),” *Defence Technology* **23**, 19–34 (2023).

²⁰Y. Huang, S. Chen, and X. Chen, “Pressure-time history prediction for fully and partially confined explosions by combining physical and deep learning models,” *Engineering Structures* **339**, 120575 (2025).

²¹Q. Li, Z. Wang, L. Li, H. Hao, W. Chen, and Y. Shao, “Machine learning prediction of structural dynamic responses using graph neural networks,” *Computers & Structures* **289**, 107188 (2023).

²²J. Hu, Z. Dou, and W. Zhang, “Fast fluid-structure interaction simulation method based on deep learning flow field modeling,” *Physics of Fluids* **36**, 120575 (2024).

²³Z. Feng, Z. Tariq, X. Shen, B. Yan, X. Tang, and F. Zhang, “An encoder-decoder convlstm surrogate model for simulating geological co2 sequestration with dynamic well controls,” *Gas Science and Engineering* **125**, 205314 (2024).

²⁴I. Flood, B. T. Bewick, R. J. Dinan, and H. A. Salim, “Modeling blast wave propagation using artificial neural network methods,” *Advanced Engineering Informatics* (2009), 10.1016/j.aei.2009.06.005.

²⁵A. M. Remennikov and T. A. Rose, “Predicting the effectiveness of blast wall barriers using neural networks,” *International Journal of Impact Engineering* **34**, 1907–1923 (2007).

²⁶W. Peng, M. Pan, C. Leng, S. Wang, and W. Z. and, “Blast loading prediction in a typical urban environment based on bayesian deep learning,” *Engineering Applications of Computational Fluid Mechanics* **19**, 2445765 (2025), <https://doi.org/10.1080/19942060.2024.2445765>.

²⁷S. Rigby, D. Smyl, A. Dennis, and J. Pannell, “Prediction of blast loading in an internal environment using artificial neural networks,” *International*

- Journal of Protective Structures **12** (2020), 10.1177/2041419620970570.
- ²⁸A. A. Dennis and S. E. Rigby, “The direction-encoded neural network: A machine learning approach to rapidly predict blast loading in obstructed environments,” *International Journal of Protective Structures* **15**, 455–483 (2024), © The Author(s) 2023. This article is distributed under the terms of the Creative Commons Attribution 4.0 License (<https://creativecommons.org/licenses/by/4.0/>) which permits any use, reproduction and distribution of the work without further permission provided the original work is attributed as specified on the SAGE and Open Access page (<https://us.sagepub.com/en-us/nam/open-access-at-sage>).
- ²⁹M. A. Kang and C. H. Park, “Prediction of peak pressure by blast wave propagation between buildings using a conditional 3d convolutional neural network,” *IEEE Access* **11**, 26114–26124 (2023).
- ³⁰G. Covoni, F. Montomoli, V. L. Tagarielli, V. Bisio, S. Rossin, and M. Ruggiero, “Application of graph neural networks to predict explosion-induced transient flow,” *Advanced Modeling and Simulation in Engineering Sciences* (2024), 10.1186/s40323-024-00272-4.
- ³¹Z. Wang, J. Peng, J. Hu, M. Wang, X. Rong, L. Bian, M. Wang, Y. He, and W. Wu, “Blastgraphnet: An intelligent computational method for the precise and rapid prediction of blast loads on complex 3d buildings using graph neural networks,” *Engineering* **49**, 205–224 (2025).
- ³²Q. Li, Z. Wang, W. Chen, L. Li, and H. Hao, “Advancing blast fragmentation simulation of rc slabs: A graph neural network approach,” *Engineering Structures* **308**, 118009 (2024).
- ³³M. A. Badjadi, H. Zhu, P. Zhao, F. Zhang, D. Hou, L. Huang, and M. Micheal, “Hybrid cnn-lstm model for predicting wettability alterations in shale reservoir based on experimental techniques,” *Geoenergy Science and Engineering* **257**, 214217 (2026).
- ³⁴Y. Wang, H. Wu, J. Zhang, Z. Gao, J. Wang, P. S. Yu, and M. Long, “Predrnn: A recurrent neural network for spatiotemporal predictive learning,” *IEEE Transactions on Pattern Analysis and Machine Intelligence* **45**, 2208–2225 (2023).
- ³⁵Y. Wang, L. Jiang, M. Yang, L. Li, M. Long, and L. Fei-Fei, “Eidetic 3d LSTM: A model for video prediction and beyond,” in *7th International Conference on Learning Representations, ICLR 2019, New Orleans, LA, USA, May 6-9, 2019* (OpenReview.net, 2019).
- ³⁶O. Ronneberger, P. Fischer, and T. Brox, *U-Net: Convolutional Networks for Biomedical Image Segmentation* (Springer International Publishing, 2015).
- ³⁷T. Sainath, O. Vinyals, A. Senior, and H. Sak, “Convolutional, long short-term memory, fully connected deep neural networks,” in *ICASSP* (2015).
- ³⁸Y. Huang, S. Zhu, and S. Chen, “Deep learning-driven super-resolution reconstruction of two-dimensional explosion pressure fields,” *Journal of Building Engineering* **78**, 107620 (2023).
- ³⁹S. Woo, J. Park, J. Lee, and I. S. Kweon, “CBAM: convolutional block attention module,” *CoRR abs/1807.06521* (2018), 1807.06521.
- ⁴⁰C. Szegedy, S. Ioffe, V. Vanhoucke, and A. Alemi, “Inception-v4, inception-resnet and the impact of residual connections on learning,” *Proceedings of the AAAI Conference on Artificial Intelligence* **31** (2017), 10.1609/aaai.v31i1.11231.
- ⁴¹X. Shi, Z. Gao, L. Lausen, H. Wang, D. Yeung, W. Wong, and W. Woo, “Deep learning for precipitation nowcasting: A benchmark and a new model,” *CoRR abs/1706.03458* (2017), 1706.03458.
- ⁴²Z. Li, N. Kovachki, K. Azizzadenesheli, B. Liu, K. Bhattacharya, A. Stuart, and A. Anandkumar, “Fourier neural operator for parametric partial differential equations,” (2021), arXiv:2010.08895 [cs.LG].
- ⁴³Y. Wang, L. Jiang, M.-H. Yang, L.-J. Li, M. Long, and L. Fei-Fei, “Eidetic 3d LSTM: A model for video prediction and beyond,” in *International Conference on Learning Representations* (2019).